Nano-optical imaging of WSe_{2} waveguide modes revealing light-exciton interactions

Z. Fei, M. E. Scott, D. J. Gosztola, J. J. Foley, IV, J. Yan, D. G. Mandrus, H. Wen, P. Zhou, D. W. Zhang, Y. Sun, J. R. Guest, S. K. Gray, W. Bao, G. P. Wiederrecht, and X. Xu

Phys. Rev. B **94**, 081402 — Published 1 August 2016

DOI: 10.1103/PhysRevB.94.081402

Nano-optical imaging of WSe_2 waveguide modes revealing light-exciton interactions

Z. Fei[1,2], M. Scott[3], D. J. Gosztola[1], J. J. Foley[1], J. Yan[4,5], D. G. Mandrus[4,5], H. Wen[6], P. Zhou[7], D. W. Zhang[7], Y. Sun[1], J. R. Guest[1], S. K. Gray[1], W. Bao[7], G. P. Wiederrecht[1], X. Xu[3,8]

[1]Center for Nanoscale Materials, Argonne National Laboratory, Lemont, Illinois 60439, USA
[2]Department of Physics and Astronomy, Iowa State University, Ames, Iowa 50011, USA
[3]Department of Physics, University of Washington, Seattle, Washington 98195, USA
[4]Materials Science and Technology Division, Oak Ridge National Laboratory, Oak Ridge, Tennessee 37831, USA
[5]Department of Materials Science and Engineering, University of Tennessee, Knoxville, Tennessee 37996, USA
[6]Advanced Photon Source, Argonne National Laboratory, 9700 South Cass Ave., Argonne, IL 60439
[7]State Key Laboratory of ASIC and System, Department of Microelectronics, Fudan University, Shanghai 200433, China
[8]Department of Materials Science and Engineering, University of Washington, Seattle, Washington 98195, USA

Abstract

We report on nano-optical imaging study of WSe_2 thin flakes with the scanning near-field optical microscopy (NSOM). The NSOM technique allows us to visualize in real space various waveguide photon modes inside WSe_2. By tuning the excitation laser energy, we are able to map the entire dispersion of these waveguide modes both above and below the A exciton energy of WSe_2. We found that all the modes interact strongly with WSe_2 excitons. The outcome of the interaction is that the observed waveguide modes shift to higher momenta right below the A exciton energy. At higher energies, on the other hand, these modes are strongly damped due to adjacent B excitons or band edge absorptions. The mode-shifting phenomena are consistent with polariton formation in WSe_2.

Main Text

Group VI transition-metal dichalcogenides (TMDCs) with chemical formula MX_2 (M = Mo, W; X = S, Se, Te) are novel semiconductors with layered structures and remarkable (opto)electronic properties [1-4]. Light-matter interactions in this class of materials have been widely explored in the far-field regime where many intriguing optical phenomena due to excitons were observed by emission and reflection/absorption spectroscopy [3-20]. Recently, a few near-field emission studies of TMDCs were reported where nanoscale photoluminescence responses due to grain boundaries were observed [21,22]. Nevertheless, near-field reflection/absorption studies that address

finite-momentum light-matter interactions are still missing. Here we perform near-field nano-optical imaging studies of WSe_2 thin flakes in the reflection mode by using the aperture-type near-field scanning optical microscopy (NSOM). With this technique, we directly excited finite-momentum waveguide photon modes inside TMDCs and studied their interactions with excitons without the need of additional momentum coupling methods.

The samples studied in our work are thin flakes of tungsten diselenide (WSe_2) – a prototypical TMDC [17-19]. The direct excitons of bulk WSe_2 are located around 1.57 eV (A excitons) and 2.03 eV (B excitons) corresponding to excitation wavelengths (λ_0) of about 790 nm and 610 nm, respectively (Fig. S3). As illustrated in Fig. 1a,b, a laser beam is delivered through the NSOM tip with an aperture of ~100 nm in diameter to excite the WSe_2 sample underneath the tip. Our laser is a tunable Ti:sapphire oscillator operating in the continuous-wave mode that covers a wide spectral range in the visible and near-infrared regime (700-950 nm). We collect all the reflected or scattered photons through an objective (N.A. = 0.45) above the sample (Fig. 1b) and these photons are counted with an avalanche photodiode (Supplementary Material). Throughout the imaging experiments, we keep the tip and objective fixed and only scan the sample stage. The NSOM collects both the topography and near-field optical images simultaneously at ambient conditions.

The sample investigated in Fig. 1 is a WSe_2 flake with a thickness of 260 nm sitting on a standard SiO_2/Si wafer (Fig. S1). By tuning λ_0, we are able to perform spectroscopic nano-imaging of the WSe_2 sample. The selective dataset of the near-field images is shown in Fig. 1c-f, where we plot the normalized photon counts. We first consider the near-field image taken at λ_0 = 900 nm (Fig. 1c). Here, we observe bright fringes on both WSe_2 and SiO_2 parallel to the sample edge (white dashed line), but the fringe pattern and intensity are clearly different on the two materials. Compared to the fringes on SiO_2, those on WSe_2 are stronger in intensity and more densely distributed. Moreover, the fringes on WSe_2 extend further away from the sample edge and demonstrate no significant damping. As a result, we are able to see fringes (upper right corner) due to a remote edge of WSe_2 that is not present within the field of view (Fig. S1b). As λ_0 decreases (Fig. 1d-f), the intensity of the fringes on WSe_2 drops rapidly indicating that their damping becomes significantly larger at shorter λ_0. Eventually at λ_0 = 760 nm (Fig. 1f), the fringes almost disappear in the interior of the sample. In contrast, fringes on SiO_2 show more subdued variations with λ_0.

The observed fringe patterns on both WSe_2 and SiO_2 can be understood to be formed due to interference between photons collected by the objective from different paths. The two major paths relevant here are sketched in Fig. 1b. In path one (P_1), photons are directly reflected off the sample and collected by the objective. In path two (P_2), photons transfer into in-plane propagative modes and scatter back to photons after reaching the sample edge. Note that the in-plane modes contributing to P_2 are mainly those propagating normal to the sample edge (along the $-x$ direction in Fig. 1b). The photons

scattered from in-plane modes propagating along other directions will not be efficiently collected by the top objective (Supplementary Material). In addition to P_1 and P_2, there are also other possible photon paths, but they play less significant roles here (Supplementary Material). As will be discussed in detail below, these in-plane modes inside path P_2 on the sample side are a mixture of photons in air or SiO_2 and confined waveguide modes inside WSe_2. The latter are enabled by the sub-diffraction-limit aperture of the NSOM tip, which generates a wide range of in-plane momenta (q). The phase difference between collected photons from paths P_1 and P_2 is determined by the distance (x) between the tip and the sample edge. Therefore when scanning the tip away from the sample edge, one expects interference fringes with periodicities that equal to the wavelengths (λ_p) of the in-plane modes. The longest distance away from the edge that the fringes extend is determined by the propagation lengths (L_p) of these modes.

Based on the above picture, we are able to determine all the essential parameters of the in-plane modes by analyzing the fringe patterns. In Fig. 2a, we plot the line profiles extracted perpendicular to the fringes of WSe_2 and SiO_2 along the arrows marked in Fig. 1d (λ_0 = 850 nm). One can see that the fringe profile of WSe_2 consists of a number of oscillations that extend far away from the sample edge (x = 0). In order to estimate L_p, we plot in Fig. 2b background-subtracted fringe profile of WSe_2 as well as calculated decay curves considering different L_p (dashed curves, see Supplementary Material for details about the calculation). The best match to the data is obtained when $L_p \approx 3$ μm (black dashed curves). As detailed below, the oscillations on WSe_2 are due to a mixture of multiple in-plane modes, so our estimation produces an average L_p over all the modes launched by the NSOM tip. Similar analysis is also performed on data profiles taken at other λ_0 (Fig. S4a). Thus-obtained $L_p(\lambda_0)$ is plotted in Fig. 2c as hollow squares, where one can see that L_p increases rapidly with λ_0 above the A exciton wavelength ($\lambda_{ex} \approx 790$ nm). The trend of the rapid increase projects to a huge L_p of tens of microns as λ_0 approaches 900 nm. Therefore, a much larger crystal with a scale over 100 μm is necessary to accurately determine L_p at wavelengths close to 900 nm. Nevertheless, the large L_p at these wavelengths is reflected by the weakly-damped fringes shown in the data image (Fig. 1c) and profiles (Fig. S4a) of our current sample with a practical size (Fig. S1b). In Fig. 2c, we also plot the theoretical calculation of the upper limit of L_p at our λ_0 range (Supplementary Material), which captures well the trend of the experimental data points.

From Fig. 2a, we notice that the fringe profile of WSe_2 is complicated and appears to be a superposition of oscillations with different periodicities. In order to determine the periodicities accurately, we performed Fourier analysis on these real-space profiles. The outcomes are the q-space profiles (Fig. 2d,e), where the peaks correspond directly to momenta ($q_p = 2\pi/\lambda_p$) of the in-plane modes. From Fig. 2d, one can see that the q-profile of SiO_2 has one broad peak close to $k_0 = 2\pi/\lambda_0$ indicating that they are mainly photons (see Supplementary Material for more discussions about bare substrate modes). The q-profile of WSe_2, on the other hand, shows multiple peaks (mark with arrows). The two

peaks close to k_0 (black arrow) and $n_{sub}k_0$ (purple arrow, n_{sub} = 1.46 is the refractive index of SiO_2) are air and substrate modes respectively. The field of the two modes are not confined inside WSe_2 but extending to air or substrate [23]. In addition to the two modes, there are three more peaks above $1.46k_0$ (blue, green and red arrows), which we label as various waveguide modes inside WSe_2 according to our dispersion analysis (see discussions below). Note that the mode at $q_p = 1.6k_0$ (blue arrow) merges with the adjacent substrate mode (purple arrow) and becomes a shoulder feature. The highest q_p of these waveguide modes is close to $2.5k_0$, corresponding to a λ_p of about 350 nm. In order to study the λ_0-dependence of the in-plane modes inside WSe_2, in Fig. 2e we plot a complete set of q-profiles of WSe_2 at all λ_0. Here, one can see that all the modes (marked with arrows) evolve systematically with λ_0. As λ_0 decreases from 900 nm towards 800 nm, all the modes shift to larger q indicating smaller mode wavelength (λ_p). When λ_0 reaches the A exciton wavelength ($\lambda_{ex} \approx 790$ nm) and below, the air and substrate modes (black and purple arrows) shift abruptly to lower q. The waveguide modes inside WSe_2 (blue, green and red arrows), on the other hand, become damped and are thus not clearly distinguishable. As λ_0 approaches 740 nm away from the A exciton, we observe a broad hump feature below $q = 2.0k_0$ (orange arrows in Fig. 2e and Fig. S4b). Such a hump feature are formed due to the merging of all the damped waveguide modes inside WSe_2 (see discussions below).

To gain insights into these modes, in Fig. 3a,b,d,e we plot the calculated λ_0- and q-dependent dispersion diagrams of the entire sample/substrate system. Because the aperture-type NSOM probe induce strong enhancement of both in-plane and out-of-plane fields, it can couple to both transverse electric (TE) and transverse magnetic (TM) modes [24,25]. Therefore we considered both TE and TM polarizations in our calculations. The dispersion diagrams in Fig. 3a,d are calculated with the realistic in-plane dielectric function of WSe_2 from literature [26], while those in Fig. 3b,e are calculated with artificial optical constants considering only the A excitons (Fig. S3). Details about the dispersion calculation and the optical constants of WSe_2 are introduced in the Supplementary Material. The bright curves shown in these dispersion plots correspond to various in-plane modes inside the system, among which we label the waveguide modes of WSe_2 as TE_0, TE_1, TE_2, TM_0 and TM_1 modes based on the calculated field distributions (Fig. 3c,f). There are also modes appearing at low q regime close to k_0 and $1.46k_0$ in the TM dispersion maps, which are air and substrate modes respectively. The data points overlaid on top the color maps in Fig. 3a,d are the q positions for the air mode (black), substrate mode (purple) and various WSe_2 waveguide modes (red, blue and green) extracted from the Fourier-q profiles in Fig. 2e. Note that we only show data points at selective λ_0 in Fig. 3a,d to avoid blocking the color map.

From Fig. 3 one can see that all the modes show distinct dispersion properties due to their coupling with the A excitons (λ_{ex}) in WSe_2 (marked with white dashed lines in the dispersion plots). More specifically, when approaching excitons from higher excitation wavelengths ($\lambda_0 > \lambda_{ex}$) all the waveguide modes inside WSe_2 shift to higher q, which can

be seen clearly from both experimental data points and calculated dispersion color plots with realistic optical constants (Fig. 3a,d). At lower excitation wavelengths ($\lambda_0 < \lambda_{ex}$), on the other hand, all the waveguide modes suffer from damping due to adjacent B excitons or band-edge absorption of WSe_2 (Fig. S3). As a result, lower branches of these waveguide modes ($\lambda_0 < \lambda_{ex}$) are not clearly resolved experimentally. Instead, they merge together as one broad hump feature (Fig. 2e). Calculations considering only the A excitons show clearer the bottom branches (Fig. 3b,e). From the dispersion color plots (Fig. 3a,b,d,e), one can see clear anti-crossing behaviors above and below λ_{ex} for all the waveguide modes, which are signatures of the formation of exciton polaritons – hybrid modes between photons and excitons [27-30]. Recently, exciton polaritons in TMDCs drew a lot of research interests [31-34] and were observed by far-field spectroscopy with cavity coupling methods [33,34]. Our real-space nano-imaging data clearly capture the high-λ_0 (or low-energy) portion of the polariton dispersion of WSe_2 (Fig. 3a,d). In addition to the waveguide modes inside WSe_2, the air and substrate modes (black and purple data points in Fig. 3d) also couple to the WSe_2 excitons and thus become discontinuous above and below λ_{ex}. For the bare SiO_2/Si substrate, on the other hand, only straight photon modes between k_0 and $1.46k_0$ can be seen in their Fourier q profiles (Fig. S5b) and also the calculated dispersion diagrams (Fig. S6). Note that the TE_0 and TM_0 modes of the 260-nm-thick WSe_2 (Fig. 3a,d) are not clearly resolved experimentally from the Fourier q profiles (Fig. 2d,e) due to their narrow linewidths that are beyond the resolution limit of our NSOM probe (Supplementary Material).

Finally, we wish to discuss the dependence of the waveguide modes with the flake thickness. In Fig. 4a, we plot the near-field image of a 120-nm-thick WSe_2 flake taken at $\lambda_0 = 850$ nm. Following the same procedure as described above, we plot in Fig. 4b the real-space fringe profile (top panel) and the corresponding Fourier q-profile (bottom panel) of WSe_2. Unlike the 260-nm-thick flake discussed above, the current thinner sample has only two peaks at $q \approx 1.6k_0$ and $2.4k_0$ (grey and yellow arrows) above the far-field photon line ($q = k_0$). Similar analysis was also done on data taken from a 70-nm-thick flake (Fig. S7), where the two peaks shift down to $q \approx 1.5k_0$ and $2.0k_0$, respectively. As the sample gets even thinner down to a few nanometers (Fig. S8), the fringes appear to be sinusoid indicating that only single mode is involved. For example, the WSe_2 samples with a thickness of 8 nm and 4 nm have mode momenta of $q \approx 1.5k_0$ and $1.3k_0$, respectively (Supplementary Material).

To understand the observed thickness dependence, we plot in Fig. 4c,d the calculated thickness- and momentum-dependent color maps of both TE and TM modes at $\lambda_0 = 850$ nm, where the bright curves represent various modes in the system. The data points here are mode positions above $q = 1.46k_0$ extracted from mode analyses from multiple samples (Fig. 2, Fig. 4, Fig. S7, Fig. S8), and they are consistent with the calculated color plots. From Fig. 4c,d, one can see that both the mode position and the number of modes evolve systematically with the flake thickness. For the 260-nm-thick flake, there are five waveguide modes above $1.46k_0$, among which the TE_1, TE_2 and TM_1 modes are clearly

resolved by our Fourier analysis (Fig. 2d). While in the case of the WSe_2 flakes with a thickness of 120 nm and 70 nm, there are two waveguide modes (TE_0 and TM_0 modes) above $1.46k_0$ (Fig. 4c,d). The TE_1 mode here in the thinner flake is below $1.46k_0$, so it merged with the air and substrate modes. When the sample gets even thinner (a few nanometers thick), only the TE_0 mode exists, which is captured by our nano-optical imaging data (Fig. S8).

With the state-of-the-art near-field optical microscopy, we performed the first nano-optical imaging study of waveguide modes inside WSe_2. By recording and analyzing the interference fringes of these modes, we were able to extract both their wavelengths and propagation lengths. We found that the wavelengths of these modes are as low as 300 nm that are 2-3 times smaller than the excitation laser wavelengths and they can propagate over tens of microns below the A exciton energy. Moreover, we observed signatures of coupling between waveguide photon modes with A excitons in WSe_2. The coupling shift the waveguide modes towards higher momenta below the A exciton energy. As the excitation laser energy increases above the A exciton energy, all waveguide modes become strongly damped due to adjacent B excitons and band-edge absorption. Our work opens up a new regime for studying light-matter interactions in TMDCs and thus provides guidelines for future applications of this class of materials in nanophotonics and optoelectronics.

Acknowledgements

This work was performed, in part, at the Center for Nanoscale Materials, a U.S. Department of Energy Office of Science User Facility under Contract No. DE-AC02-06CH11357.

References

[1] B. Radisavljevic, A. Radenovic, J. Brivio, V. Giacometti, A. Kis, Nat. Nanotechnol. **6**, 147-150 (2011).

[2] Q. H. Wang, K. Kalantar-Zadeh, A. Kis, J. N. Coleman, M. S. Strano, Nat. Nanotechnol. **7**, 699-712 (2012).

[3] K. F. Mak, C. Lee, J. Hone, J. Shan, T. F. Heinz, Phys. Rev. Lett. **105**, 136805 (2010).

[4] A. Splendiani, L. Sun, Y. Zhang, T. Li, J. Kim, C.-Y. Chim, G. Galli, and F. Wang, Nano Lett. **10**, 1271-1275 (2010).

[5] K. F. Mak, K. He, C. Lee, G. H. Lee, J. Hone, and T. F. Heinz, Nat. Mater. **12**, 207-211 (2013).

[6] K. F. Mak, K. He, J. Shan, and T. F. Heinz, Nat. Nanotechnol. **7**, 494-498 (2012).

[7] H. Zeng, J. Dai, W. Yao, D. Xiao, and X. Cui, Nat. Nanotechnol. **7**, 490-493 (2012).

[8] H. Shi, R. Yan, S. Bertolazzi, J. Brivio, B. Gao, A. Kis, D. Jena, H. G. Xing, and L. Huang, ACS Nano **7**, 1072-1080 (2013).

[9] J. S. Ross, S. Wu, H. Yu, N. J. Ghimire, A. M. Jone, G. Aivazian, J. Yan, D. G. Mandrus, D. Xiao, W. Yao, and X. Xu, Nature Commun. **4**, 1474 (2013).

[10] Jones, A. M.; Yu, H.; Ghimire, N. J.; Wu, S.; Aivazian, G.; Ross, J. S.; Zhao, B.; Yan, J.; Mandrus, D. G.; Xiao, D.; Yao, W.; Xu, X, *Nat. Nanotech.* **2013**, 8, 634-638.
[11] Q. Cui, F. Ceballos, N. Kumar, and H. Zhao, ACS Nano **3**, 2970-2976 (2014).
[12] Z. Nie, R. Long, L. Sun, C.-C. Huang, J. Zhang, Q. Xiang, D. W. Hewak, Z. Shen, O. V. Prezhdo, and Z.-H. Loh, ACS Nano **10**, 10931-10940 (2014).
[13] Z. Ye, T. Cao, K. O'Brien, H. Zhu, X. Yin, Y. Wang, S. G. Louie, and X. Zhang, Nature **513**, 214-218 (2014).
[14] H.-L. Liu, C.-C. Shen, S.-H. Su, C.-L. Hsu, M.-Y. Li, and L.-J. Li, Appl. Phys. Lett. **105**, 201905 (2014).
[15] X. Hong, J. Kim, S.-F. Shi, Y. Zhang, C. Jin, Y. Sun, S. Tongay, J. Wu, Y. Zhang, and F. Wang, Nat. Nanotechnol. **9**, 682-686 (2014).
[16] X. Xu, W. Yao, D. Xiao, and T. F. Heinz, Nature Phys. **10**, 343-350 (2014).
[17] H. Fang, S. Chuang, T. C. Chang, K. Takei, T. Takahashi, and A. Javey, Nano Lett. **12**, 3788-3792 (2012).
[18] J. S. Ross, P. Klement, A. M. Jone, N. J. Ghimire, J. Yan, D. G. Mandrus, T. Taniguchi, K. Watanabe, K. Kitamura, W. Yao, D. H. Cobden, and X. Xu, Nat. Nanotechnol. **9**, 268-272 (2014).
[19] S. Wu, S. Buckley, J. R. Schaibley, L. Feng, J. Yan, D. G. Mandrus, F. Hatami, W. Yao, J. Vučković, A. Majumdar, and X. Xu, Nature **520**, 69-72 (2015).
[20] M. Amani, D.-H. Lien, D. Kiriya, J. Xiao, A. Azcatl, J. Noh, S. R. Madhvapathy, R. Addou, S. KC, M. Dubey, K. Cho, R. M. Wallace, S.-C. Lee, J.-H. He, J. W. Ager III, X. Zhang, E. Yablonovitch, and A. Javey, Science **350**, 1065-1068 (2015).
[21] W. Bao, N. J. Borys, C. Ko, J. Suh, W. Fan, A. Thron, Y. Zhang, A. Buyanin, J. Zhang, S. Cabrini, P. D. Ashby, A. Weber-Bargioni, S. Tongay, S. Aloni, D. F. Ogletree, J. Wu, M. B. Salmeron and P. J. Schuck, Nat. Commun. **6**, 7993 (2015).
[22] Y. Lee, S. Park, H. Kim, G. H. Han, Y. H. Lee, and J. Kim, Nanoscale, **7**, 11909 (2015).
[23] R. G. Hunsperger, Integrated optics. Chapter 2. Optical waveguide modes. (Springer Science + Business Media, LLC 2009).
[24] A. Drezet, M. J. Nasse, S. Huant, and J. C. Woehl, Europhys. Lett. **66**(1), 41-47 (2004).
[25] A. M. Mintairov, Y. Chu, Y. He, S. Blokhin, A. Nadtochy, M. Maximov, V. Tokranov, S. Oktyabrsky, and J. L. MerzA, Phys. Rev. B **77**, 195322 (2008).
[26] R. Beal, W. Y. Liang, and H. P. Hughes, J. Phys. C: Solid State Phys. **9**, 2449-2457 (1976).
[27] C. Weisbuch, M. Nishioka, A. Ishikawa, and Y. Arakawa, Phys. Rev. Lett. **69**, 3314–3317 (1992).
[28] F. Tassone, F. Bassani, and L. C. Andreani, Phys. Rev. B **45**, 6023 (1992).
[29] H. M. Gibbs, G. Khitrova, and S. W. Koch, Nat. Photon. **5**, 275-282 (2011).
[30] H. Deng, H. Haug, and Y. Yamamoto, *Rev. Mod. Phys.* **82**, 1489 (2010).
[31] J. B. Khurgin, *Optica* **2**, 740-742 (2015).

[32] Y. N. Gartstein, X. Li, and C. Zhang, Phys. Rev. B **92**, 075445 (2015).
[33] X. Liu, T. Galfsky, Z. Sun, F. Xia, E. Lin, Y.-H. Lee, S. Kéna-Cohen, and V. M. Menon, Nat. Photon. **9**, 30-34 (2015).
[34] S. Dufferwiel, S. Schwarz, F. Withers, A. A. P. Trichet, F. Li, M. Sich, O. Del Pozo-Zamudio, C. Clark, A. Nalitov, D. D. Solnyshkov, G. Malpuech, K. S. Novoselov, J. M. Smith, M. S. Skolnick, D. N. Krizhanovskii, A. I. Tartakovskii, Nat. Commun. **6**, 8579 (2015).

Figures Captions

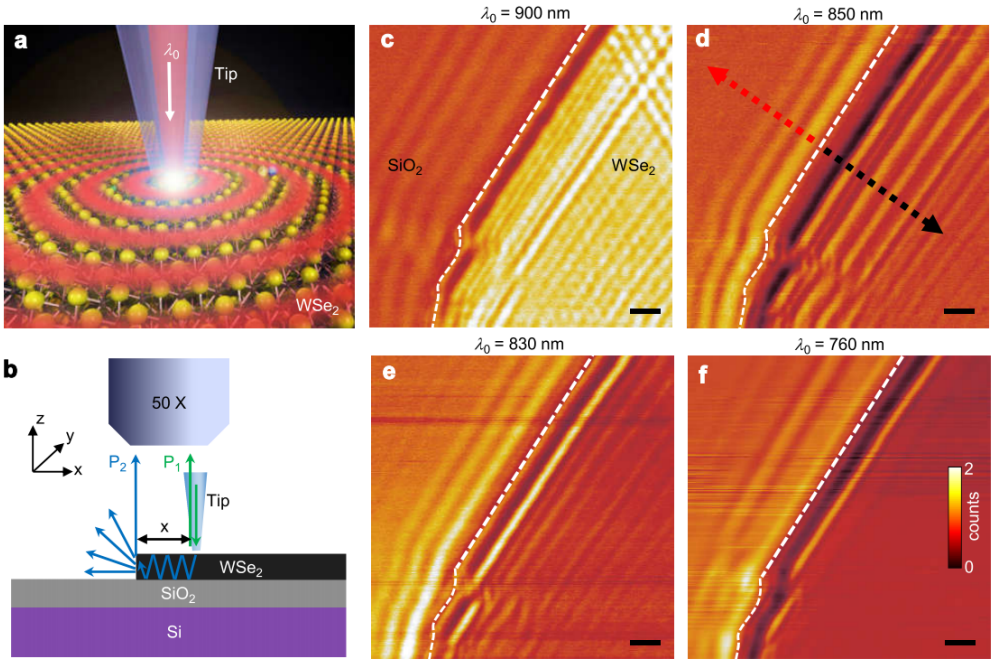

Fig. 1. a, Schematics of the near-field optical study of WSe_2. **b**, Illustration of the experimental setup and two major pathways (P_1 and P_2) that photons are collected by the top objective. **c-f**, Selected nano-optical imaging data of a WSe_2 flake (thickness = 260 nm) taken at various excitation wavelengths (λ_0). Here we plot the total counts of the photons collected by the objective normalized to that taken on the SiO_2/Si substrate. The white dashed lines mark the edges of the WSe_2 flake. The two arrows in **d** mark the directions along which we took line profiles across the fringes on both WSe_2 and SiO_2 as plotted in Fig. 2a. Scale bars in **c-f** represent 1 μm.

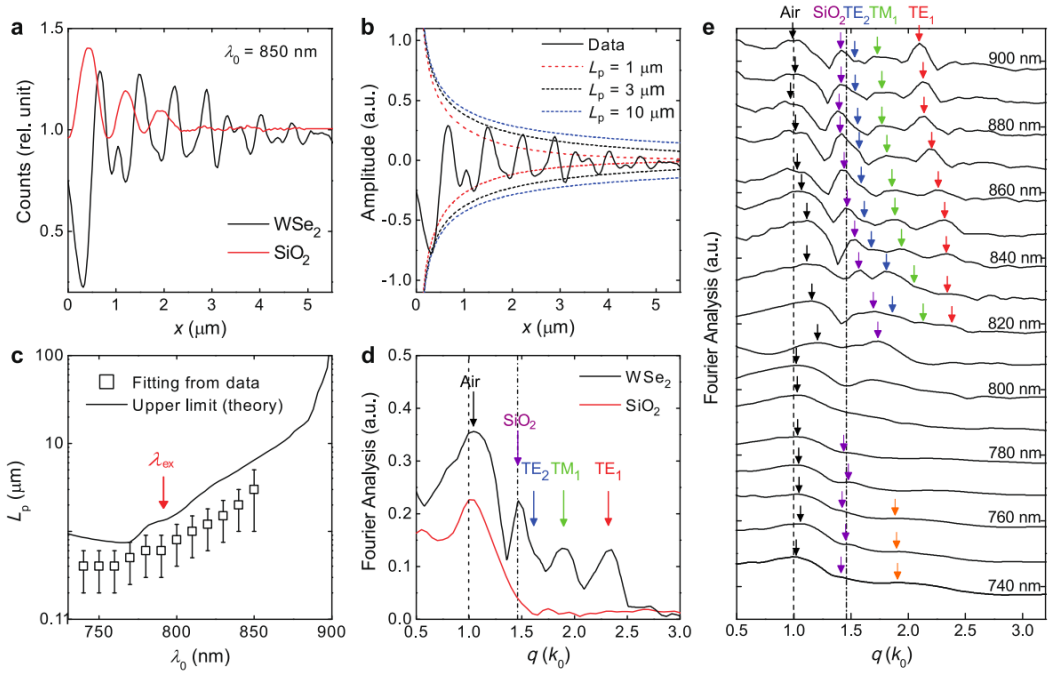

Fig. 2. a, Real-space fringe profiles of WSe_2 and SiO_2 at $\lambda_0 = 850$ nm taken directly from Fig. 1d along the black and red arrows, respectively. **b**, The same fringe profile of WSe_2 as **a** with background signal subtracted and the calculated decay curves by assuming different propagation lengths (L_p) (see Supplementary Materials). **c**, Estimated L_p versus λ_0 from data fitting (hollow squares) and theoretical calculation of the upper limit of $L_p(\lambda_0)$ (black curve, see Supplementary Materials). The red arrow marks the A exciton wavelength (λ_{ex}). **d**, Momentum (q) profiles of WSe_2 and SiO_2 at $\lambda_0 = 850$ nm obtained by Fourier analysis of the real-space fringe profiles shown in **a**. **e**, The q-profiles of WSe_2 (black curves) at all λ_0 obtained by Fourier analysis of the real-space fringe profiles (Fig. S3a). The q-profiles are displaced vertically for clarity. The unit of the q axis in **d**,**e** is the excitation far-field wavevector $k_0 = 2\pi/\lambda_0$. The vertical black dashed and dash-dotted lines in **d**,**e** mark the photon lines in air ($q = k_0$) and SiO_2 ($q = 1.46k_0$), respectively. The black and purple arrows in **d**,**e** mark the air and substrate modes. The blue, green and red arrows in **d,e** mark respectively the TE_2, TM_1 and TE_1 waveguide modes inside WSe_2. The orange arrows in **e** at low λ_0 regime mark a broad hump feature that occurs due to the merging of the damped waveguide modes.

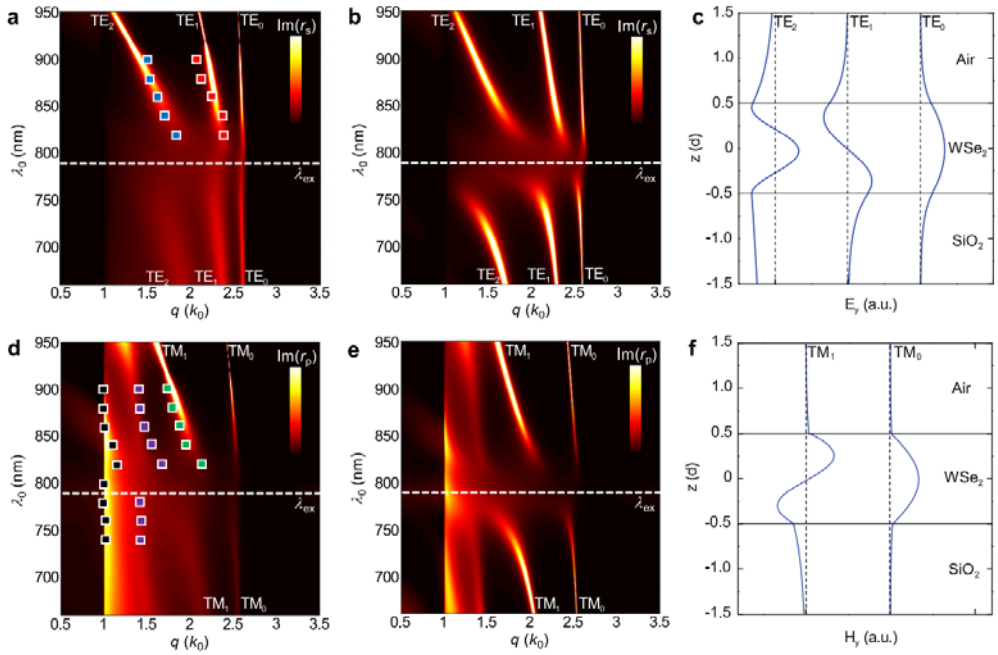

Fig. 3. **a**,**b**, Calculated color maps about the imaginary part of *s*-polarized reflection coefficient Im[$r_s(q, \lambda_0)$] of the WSe_2 sample (thickness = 260 nm) with both realistic and artificial optical constants (Fig. S3). **c**, Calculation of the *y*-direction electric field (E_y) of TE_0, TE_1 and TE_2 modes at λ_0 = 900 nm. **d**,**e**, Calculated color maps of the imaginary part of the *p*-polarized reflection coefficient Im[$r_p(q, \lambda_0)$] of the WSe_2 sample with both realistic and artificial optical constants. **f**, Calculation of the *y*-direction magnetic field (H_y) of TM_0 and TM_1 modes at λ_0 = 900 nm. The data points in **a,d** mark the peak positions extracted from the Fourier *q* profiles in Fig. 2e. To avoid blocking the color map, we only show data points at selected wavelengths (900 nm, 880 nm … 740 nm) here. The unit of the *q* axis in **a,b,d,e** is k_0. The bright curves in **a,b,d,e** above $q = 1.46k_0$ represent various waveguide modes inside WSe_2 as labeled in the figures. The horizontal dashed lines in **a,b,d,e** mark the wavelength for the A exciton of WSe_2 (λ_{ex}). The horizontal solid lines in **c**,**f** mark the air/WSe_2 and WSe_2/SiO_2 interfaces. The vertical dashed lines in **c**,**f** mark $H_y = 0$ and $E_y = 0$, respectively.

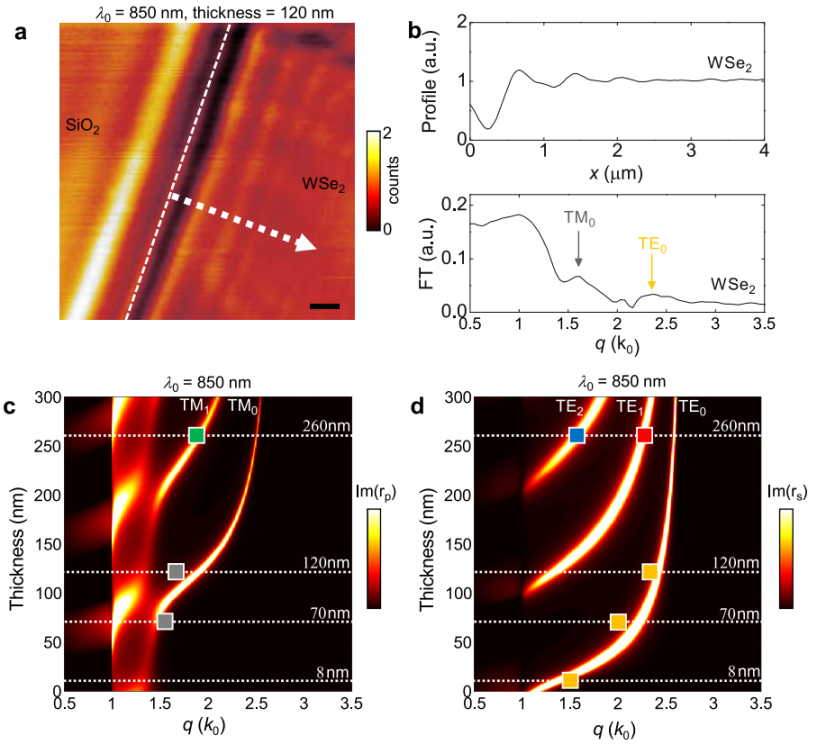

Fig. 4. a, Nano-optical imaging data of a 120-nm-thick WSe_2 thin flake taken at $\lambda_0 = 850$ nm. The white dashed line marks the edge of the WSe_2 flake. Scale bar represents 700 nm. **b**, Real-space line profile (top panel) taken along the white arrow in **a** and the corresponding q-profile (bottom panel) obtained from Fourier analysis. The arrows here mark the positions of two waveguide modes above q=1.46k_0. **c**,**d**, Calculated thickness- and momentum-dependence color maps of Im(r_p) and Im(r_s) for TM and TE modes respectively. The data points overlaid on top the color maps mark the mode positions of WSe_2 waveguide modes extracted from mode analysis in Fig. 2, Fig. 4, Fig. S7 and Fig. S8.